Computation of Aerodynamic Sound around Complex Stationary and Moving Bodies

J. H. Seo[*] and R. Mittal[†]

Department of Mechanical Engineering, Johns Hopkins University, Baltimore, MD, 21218

Aerodynamic sound generation at low Mach numbers around complex stationary and moving bodies is computed directly with an immersed-boundary method-based hybrid approach. The complex flow field is solved by the immersed-boundary incompressible Navier-Stokes flow solver and the sound generation and propagation are computed by the linearized perturbed compressible equations with a high-order immersed boundary method, on a non-body conformal Cartesian grid. The present method is applied to the prediction of noise generated by turbulent flow over a tandem cylinder arrangement as well as a rudimentary landing gear noise. For a moving body problem, the aerodynamic sound generated by modeled flapping wings is computed.

I.   Introduction

COMPUTATIONAL aeroacoustics (CAA) has been applied successfully to various aerodynamic noise problems. For example, noise generated by high-speed jet flow[1] has been been successfully tackled via the direct noise computation approach[1,2] (i.e. direct computation of full compressible Navier-Stokes equations with high-resolution numerical methods). Airframe noise[3] wherein noise is generated by the interaction between air flow and solid boundaries is a major consideration in the design of commercial aircraft. Fundamental airframe noise problems for canonical geometries and airfoils have therefore been studied by many researchers[3-9], especially employing hybrid approaches. Some practical airframe noise problems such as noise generation by the landing gear[10,11] and high-lift wing[12,13] is however still challenging, since the flow Mach number is relatively low (M<0.3) and the geometry of solid body is extremely complex. These factors make it hard to apply direct noise computation approach to those problems. The geometric complexity in particular is a major concern in the computation of the acoustic field. There have been several approaches to deal with complex geometries in CAA: a multi-block, structured grid approach[14], an overset structured grid method[15,16] and a finite-volume approach with a high-order discontinuity Galerkin method (DGM)[17-20], and an immersed boundary method (IBM)[21-25]. The first two approaches have limitations in tackling complex geometries and DGM suffers from the high computational cost. The IBM (see review[26]) is highly versatile approach to deal with complex geometries. With IBM, problems with very complex geometries can be solved on a body non-conformal Cartesian grid. Also, since it is based on the Cartesian grid, the well-established, efficient finite-difference techniques can be used.

Recently, the authors have proposed a computational methodology to solve aeroacoustic problems at low Mach numbers in complex geometry using a sharp-interface, higher-order immersed boundary method[25]. The method employs a two-step hybrid approach based on the hydrodynamic/acoustic splitting technique[27-29] for efficient computation of low Mach number aeroacoustics. In this approach, the flow field is obtained by solving the incompressible Navier-Stokes equations (INS), and the acoustic field is predicted by the linearized perturbed compressible equations (LPCE) proposed by Seo & Moon[29]. The INS/LPCE hybrid method is a two-step/one-way coupled approach to direct simulation of flow-induced noise. In the proposed method, an immersed boundary solver for incompressible flows is coupled with a new high-order IBM for solving the LPCE equations with complex immersed boundaries. This high-order IBM employs ghost-cells as in Mittal et al.[30,31] but the method is extended to higher-orders by using an approximating polynomial method originally proposed by Luo et al.[32] Dirichlet as well as Neumann boundary conditions can be applied with a high order of accuracy on the solid surface using the method. Thus dispersion/dissipation errors caused by the boundary condition formulation can be minimized, thereby ensuring highly accurate representation of wave reflection on the solid walls. As described in this paper, the method can handle stationary as well as moving bodies. In the present study, we apply this method to the computation of

---

[*] Post doctoral fellow, AIAA Member (jhseo@jhu.edu)
[†] Professor, AIAA Associate Fellow; Corresponding Author (mittal@jhu.edu)

aerodynamic sound in complex geometries associated with airframe noise for stationary as well as moving bodies. Computational methodology and procedure are described in Sec. II and several fundamental and application aerodynamic sound problems are considered in Sec. III.

II.   Computational Methods

A. Governing Equations

In the present study, aerodynamic sound at low Mach numbers is directly computed by a hybrid method based on the hydrodynamic/acoustic splitting[27,28]. In this approach, the total flow variables are decomposed into the incompressible variables and the perturbed compressible ones as,

$$\rho(\vec{x},t) = \rho_0 + \rho'(\vec{x},t)$$
$$\vec{u}(\vec{x},t) = \vec{U}(\vec{x},t) + \vec{u}'(\vec{x},t) \cdot \qquad (1)$$
$$p(\vec{x},t) = P(\vec{x},t) + p'(\vec{x},t)$$

The incompressible variables predicted by the incompressible Navier-Stokes (INS) equations represent the hydrodynamic flow field, while the acoustic fluctuations and other compressibility effects are resolved by the perturbed quantities denoted by $(')$. The incompressible Navier-Stokes equations are written as

$$\nabla \cdot \vec{U} = 0, \qquad (2)$$

$$\frac{\partial \vec{U}}{\partial t} + (\vec{U} \cdot \nabla)\vec{U} = -\frac{1}{\rho_0}\nabla P + \nu_0 \nabla^2 \vec{U} \cdot \qquad (3)$$

The perturbed quantities are obtained by solving the linearized perturbed compressible equations (LPCE)[29] with the incompressible flow solutions. A set of LPCE can be written in a vector form as,

$$\frac{\partial \rho'}{\partial t} + (\vec{U} \cdot \nabla)\rho' + \rho_0(\nabla \cdot \vec{u}') = 0 \qquad (4)$$

$$\frac{\partial \vec{u}'}{\partial t} + \nabla(\vec{u}' \cdot \vec{U}) + \frac{1}{\rho_0}\nabla p' = 0 \qquad (5)$$

$$\frac{\partial p'}{\partial t} + (\vec{U} \cdot \nabla)p' + \gamma P(\nabla \cdot \vec{u}') + (\vec{u}' \cdot \nabla)P = -\frac{DP}{Dt} \cdot \qquad (6)$$

The INS/LPCE hybrid method have well been validated for fundamental dipole/quadruple noise problems[29] and also for the turbulent noise problems[7,9]. The left hand sides of LPCE represent the effects of acoustic wave propagation and refraction in the unsteady, inhomogeneous flows, while the right hand side only contains the acoustic source term, which will be projected from the incompressible flow solution.

B. Numerical Methods

The incompressible Navier-Stokes equations (Eq. 2-3) are solved with a fractional step based method. A second-order central difference is used for all spatial derivatives and time integration is performed with the second-order Adams-Bashforth method for convection terms and Crank-Nicolson method for diffusion terms[30]. The pressure Poisson equation is solved with a multi-grid method based on a line-Gauss-Seidel (LGS) matrix solver. The LPCE are spatially discretized with a sixth-order central compact finite difference scheme[33] and integrated in time using a four-stage Runge-Kutta method. Near the immersed solid boundary and domain boundaries, third-order and fourth-order boundary schemes[33] are used. Since a central compact scheme has no dissipation error, an implicit spatial filtering proposed by Gaitnode et al.[34] is applied to suppress high frequency errors and ensure numerical stability. In this study, we applied tenth-order filtering in the interior region. Near the boundaries, successively reduced order:

from 8th to 2nd-order; filters are used. Compact finite-difference and implicit spatial filtering are solved with a tri-diagonal matrix solver.

C. Immersed Boundary Formulation

The incompressible Navier-Stokes equations for the base flow with complex immersed boundaries are solved using the sharp-interface immersed boundary method of Mittal et al.[30]. In this method, the surface of the immersed body is represented by an unstructured surface mesh which consists of triangular elements. At the pre-processing stage before integrating governing equations, all cells whose centers are located inside the solid body are identified and tagged as "body" cells and the other points outside the body are "fluid" cells. Any body-cell which has at least one fluid-cell neighbor is tagged as a "ghost-cell" (see Fig. 1a), and the wall boundary condition is imposed by specifying an appropriate value at this ghost point. In the method of Mittal et al.[30] a "normal probe" is extended from the ghost point to intersect with the immersed boundary (at a body denoted as the "body intercept"). The probe is extended into the fluid to the "image point" such that the body-intercept lies midway between the image and ghost points. A linear interpolation is used along the normal probe to compute the value at the ghost-cell based on the boundary-intercept value and the value estimated at the image-point. The value at the image-point itself is computed through a tri-linear (in 3D) interpolation from the surrounding fluid nodes. This procedure leads to a nominally second-order accurate specification of the boundary condition of the immersed boundary.
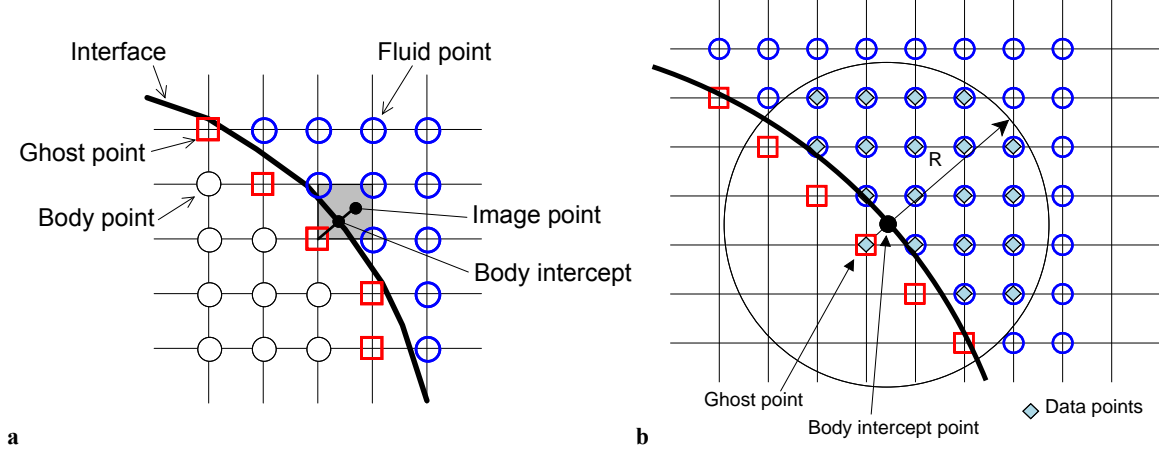
Figure 1. Schematic of ghost cell method (a) and boundary condition formulation (b).

Higher-order immersed boundary method for acoustic solver[25] is proposed using a high-order polynomial interpolation combined with a weighted-least square error minimization. In this approach, the value at the ghost point is determined by satisfying the boundary condition at the body-intercept (BI) point using high-order polynomials. Specifically, a generic variable ϕ is approximated in the vicinity of the body-intercept point (x_{BI}, y_{BI}, z_{BI}) in terms of a Nth-degree polynomial Φ as follows:

$$\phi(x',y',z') \approx \Phi(x',y',z') = \sum_{i=0}^{N}\sum_{j=0}^{N}\sum_{k=0}^{N} c_{ijk}(x')^{i}(y')^{j}(z')^{k}, \quad i+j+k \leq N \qquad (7)$$

where $x' = x - x_{BI}, y' = y - y_{BI}, z' = z - z_{BI}$ and c_{ijk} are unknown coefficients. The coefficients, c_{ijk} can be expressed as

$$c_{000} = \phi_{BI}, \quad c_{ijk} = \frac{1}{(i!)(j!)(k!)}\frac{\partial^{(i+j+k)}\phi}{\partial x^{(i)}\partial y^{(j)}\partial z^{(k)}}\bigg|_{BI}. \qquad (8)$$

The number of coefficient for third-order polynomial (N=3) is 10 for 2D and 20 for 3D. (For the full list of number of coefficient for different polynomial order, see Ref[25]). In order to determine these coefficients, we need values of ϕ from fluid data points around the body-intercept point. Following Luo et al.[32], a convenient and logical method for selected these data points is to search a circular (spherical in 3D) region (of radius R) around the body-intercept

point. (see Fig. 1b). With M such data points, the coefficients c_{ijk} can be determined by minimizing the weighted error estimated as:

$$\varepsilon = \sum_{m=1}^{M} w_m^2 \left[\Phi(x'_m, y'_m, z'_m) - \phi(x'_m, y'_m, z'_m) \right]^2 , \qquad (9)$$

where (x'_m, y'_m, z'_m) is the m-th data point, and w_m is the weight function. In this study, we used a cosine weight function suggested in the previous study[32]. To make the least-square problem well-posed, the number of data point should be larger than the number of coefficients, and the radial range R is adaptively chosen so as to ensure the satisfaction of this well-posedness condition. Since we need to find the value at the ghost point in conjunction with the body point, the first data point is replaced by the ghost point, and $(M-1)$ data points are found in fluid region (see Fig. 1b). The exact solution of the least-square problem, Eq. (9) is given by

$$\mathbf{c} = (\mathbf{WV})^+ \mathbf{W} \boldsymbol{\phi} , \qquad (10)$$

where superscript $+$ denotes the pseudo-inverse of a matrix, vector $\mathbf{c}$ and $\boldsymbol{\phi}$ contain coefficients c_{ijk} and the data $\phi(x'_m, y'_m, z'_m)$ respectively, and $\mathbf{W}$ and $\mathbf{V}$ are the weight and Vandermonde matrices. Note that (x'_1, y'_1, z'_1) is the ghost-point. After solving Eq. (10), the coefficients c_{ijk} can be written as a linear combination of $\phi(x'_m, y'_m, z'_m)$. According to Eq. (8), coefficients c_{ijk} represent the value and derivatives at the body-intercept point (x_{BI}, y_{BI}, z_{BI}) :

$$c_{000} = \phi(x_{BI}, y_{BI}, z_{BI}), \quad c_{100} = \frac{\partial \phi}{\partial x}(x_{BI}, y_{BI}, z_{BI}), \quad c_{010} = \frac{\partial \phi}{\partial y}(x_{BI}, y_{BI}, z_{BI}), \cdots. \qquad (11)$$

Therefore, for given Dirichlet or Neumann type boundary condition at the body wall, the value at the ghost point can be evaluated with Eq. (10) & (11). The more details about immersed boundary formulation can be found in the Ref[25].
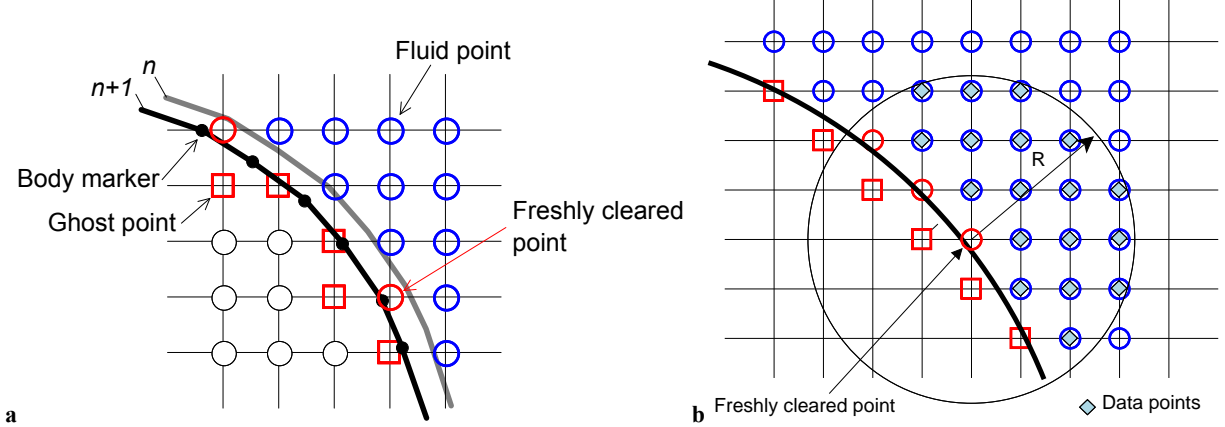
Figure 2. Schematic of moving boundary (a) and fresh cell treatment (b).

D. Freshly Cleared Cell Treatment

In the present method, the arbitrary body motion is accomplished by the displacement of each node (body-marker) of triangular surface mesh which describes the immersed body. Dealing with the moving body on the fixed grid leads the presence of 'freshly cleared cell'[35](fresh cell, hereafter) (see Fig. 2a). Since those fresh cells have no time histories of variables required to integrate the governing equations, the variable values at the fresh cell need to be obtained by the interpolation with the values at nearby cells[35]. In the present incompressible flow solver, the variable value at the new time level is evaluated by a tri-linear interpolation iteratively along with the solution of momentum equations[30]. For the acoustic solver, the value at the fresh cell is obtained by interpolation using the high-order, approximating polynomial, Eq. (7). Overall procedure is similar to the ghost cell treatment described in the section II.C, but in this case, the center for the data-point earch is the fresh cell center, (x_{FC}, y_{FC}, z_{FC}), and $x'=x-x_{FC}$, $y'=y-y_{FC}$, $z'-z_{FC}$ (see Fig. 2b). In order to avoid iterative procedure, only non-fresh, fluid cells are considered as data

points for the least square error minimization. Once the coefficients of the approximating polynomial are obtained by solving, Eq. (10), the value at the fresh cell is directly given by the first coefficient, i.e.

$$\phi(x_{FC}, y_{FC}, z_{FC}) = c_{000}.$$ (12)

III.   Result and Discussion

The present method has been well validated for sound generated by laminar flow over a single circular cylinder by comparing the results with the direct simulation of full compressible Navier-Stokes equations performed on a body-fitted grid[25]. In the present paper, the method is applied to the prediction of noise generated by turbulent flow over tandem cylinders, a configuration of interest to the problem of airframe noise. A rudimentary landing gear configuration is also considered in order to demonstrate the capability of the present method for very complex geometries. Finally, the aerodynamic sound by modeled flapping wing motion is considered as a moving body problem with relatively complex geometrical configuration.
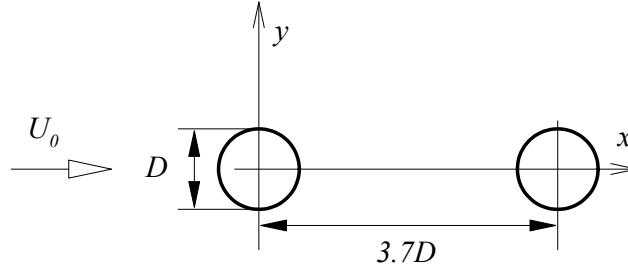
Figure 3. Schematic of two cylinders in tandem configuration.

A. Sound Generated by Turbulent Flow over Two cylinders in Tandem Configuration

The present method is applied to the sound generated by the flow over a tandem cylinder configuration shown in Fig. 3. This problem has been considered as a canonical case for airframe noise especially for the noise generated by bluff body wake interference. In this study, we perform the simulation for the case considered in the recent workshop on Benchmark Problems for Airframe Noise Computations (BANC-I, Prob. 2, Tandem Cylinders Benchmark Problem[36]). The schematic is shown in Fig. 3. The free stream velocity is U_0=44 m/s which corresponds to a Reynolds number of Re_D=1.66×10⁵. The Mach number is M=0.128, which is appropriate for the the present hybrid method. In the present computation, however, we reduce the Reynolds number to 4000. The domain size is -30D≤x≤40D, -40D≤y≤40D, and the span-wise extent L_z=3D is used and the periodic boundary condition is applied in the span-wise (z) direction. A non-uniform Cartesian grid with total 768×384×32 (9.4 million) grid points is used. The flow field is computed by the IBM incompressible flow solver and Fig. 4 shows the instantaneous vortical structure visualized by an iso-surface of the second invariant of the velocity gradient tensor

$$Q = \frac{1}{2}\left(\Omega_{ij}\Omega_{ij} - S_{ij}S_{ij}\right),$$ (13)

where Ω and S are vorticity and strain rate tensors, respectively. At the current Reynolds number (Re_D=4000) and separation distance between the cylinders, s=3.7D, the wake of upstream cylinder rolls up before it reaches the downstream cylinder and the vortex shedding of the upstream cylinder interacts with the downstream one. This overall flow behavior is similar with that reported for the higher Reynolds number[37]. Time histories of aerodynamic force coefficients are shown in Fig. 5 and the average and *rms*(root-mean-squared) values are tabulated in Table 1. As one can see on those data, aerodynamic force fluctuation is much stronger for the downstream cylinder due to the interaction with vortices shed from the upstream cylinder wake. The dominant vortex shedding frequency is found at St=0.196. It should be noted that the aerodynamic forces for the present Reynolds number (Re_D=4000) are higher than that observed in the experiment at the higher Reynolds number (Re_D=1.66×10⁵)[36-38]. The dominant shedding frequency of the present case (St=0.196) is lower than the value measured in the NASA experiments[36-38] (St=0.234), but it is close to the direct numerical simulation result of Papaioannou et al.[39](St~0.18, Re_D=1000) and the experimental measurement of Igarashi[40](St~0.19, Re_D=22000).
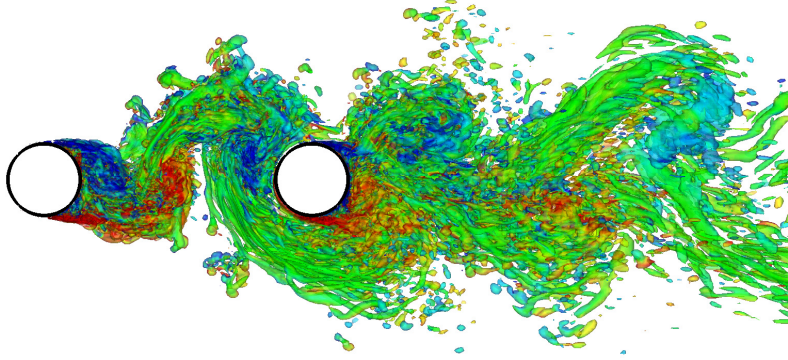
Figure 4. Vortical structure of flow over tandem cylinders. Iso-surface of Q colored by span-wise vorticity.
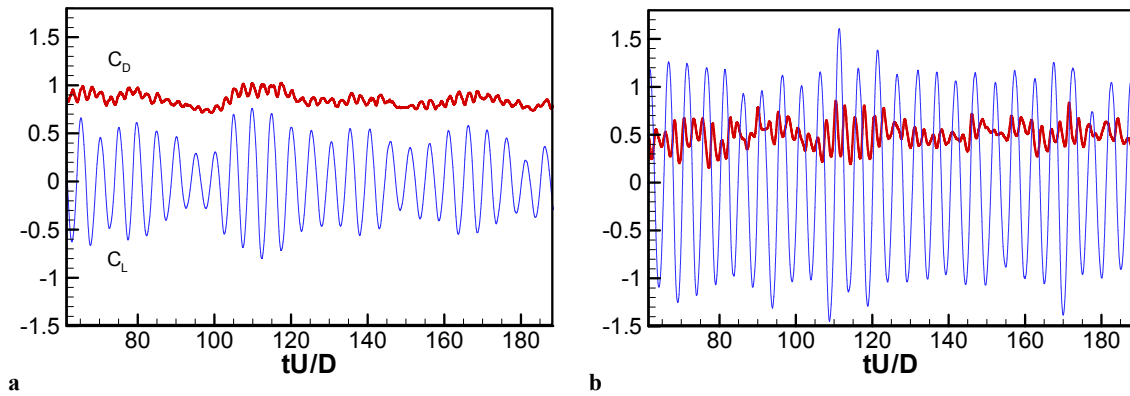
Figure 5. Time histories of aerodynamic coefficients; a) upstream cylinder, b) downstream cylinder.

Table 1. Aerodynamic coefficients

	Upstream Cylinder	Downstream Cylinder
$\overline{C}_D$	0.849	0.4948
$C_D{'}_{rms}$	0.066	0.1206
$C_L{'}_{rms}$	0.364	0.8158

The acoustic field is computed by the LPCE with the incompressible flow solutions. Although the flow computation is carried out assuming span-wise periodicity with the span-wise extent, L_z=3D, this span-wise domain size is too small for the 3D acoustic field computation, since the acoustic length scale is larger than the flow length scale at the present Mach number (M=0.128). The acoustic field computation is, therefore, performed two-dimensionally for the zero span-wise wave number component (k_z=0) which is directly related to the three-dimensional acoustic field at the span-wise center (symmetry) plane, following the approach used in the work of Seo and Moon[7]. The predicted result is then corrected for three-dimensionally using the Oberai's formulation[41]. The domain size in the *x-y* plane for the acoustic field computation is the same as the flow field, but a different Cartesian grid with 500×400 grid points is used. The acoustic grid resolution is about two-times coarser than the flow one at the near field, while it is little bit finer at the far field in order to resolve acoustic waves of higher frequencies accurately. The 3D flow field result averaged in span-wise direction is interpolated onto the acoustic grid. The instantaneous acoustic field is shown in Fig. 6a. The wave length corresponding to the dominant frequency is about 40.5D, and the high frequency components caused by turbulent fluctuation are also visible in the dilatation rate contours. The acoustic pressure is monitored at three locations: **A**(-8.33D,27.815D), **B**(9.11D,32.49D), and **C**(26.55D,27.815D), which were the microphone positions in the NASA tandem cylinder experiment. Power spectral densities (PSD) of acoustic pressure fluctuation at these three locations are plotted in Fig. 6b. The spectrum is corrected to the three dimensional one at the center plane[7]. The spectra can be characterized with broadened tones

and the significant peaks at the harmonics of the dominant frequency, which is in the qualitative agreement with the measured data[38].
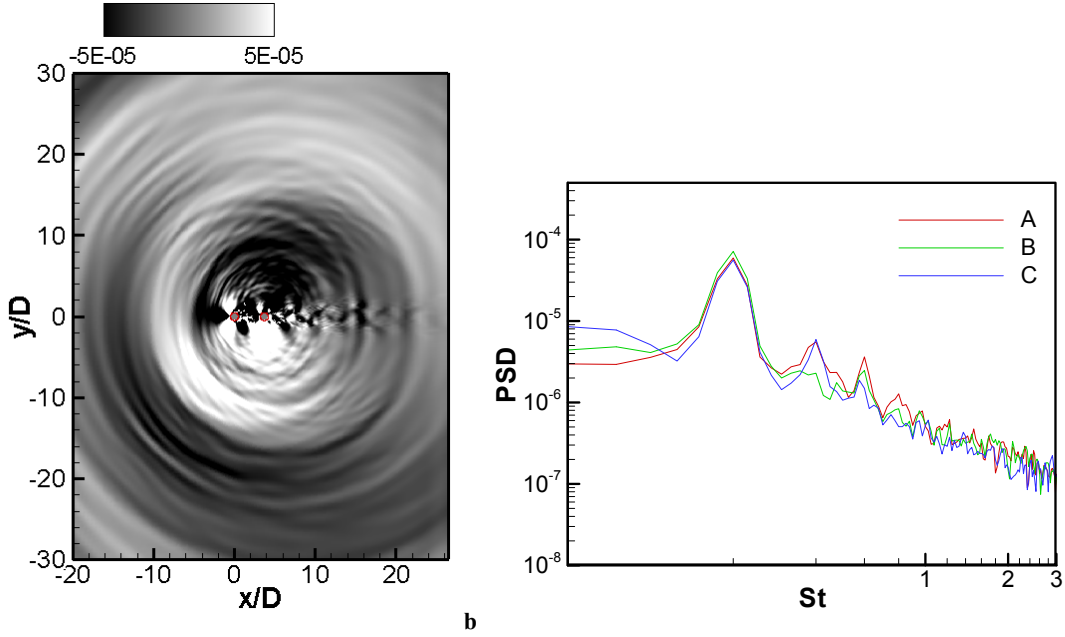
Figure 6. a) Instantaneous acoustic field (dilatation rate, $\nabla \cdot \vec{u}\,'$ contour). b) Power spectral densities (PSD) of acoustic pressure monitored at three locations : A(-8.33D,27.815D), B(9.11D,32.49D), and C(26.55D,27.815D).
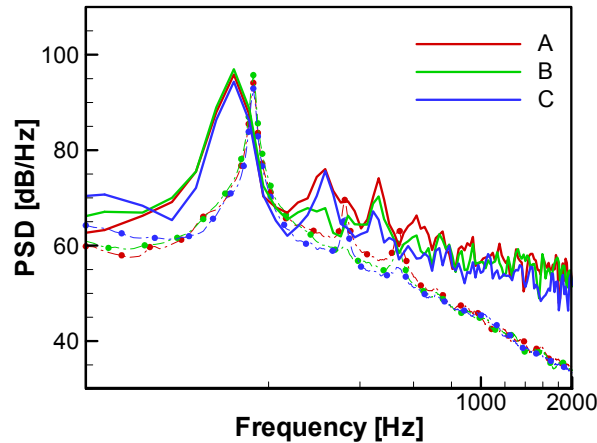
Figure 7. PSDs corrected for actual long span (16D) at three locations: A(-8.33D,27.815D), B(9.11D,32.49D), and C(26.55D,27.815D). Solid lines: Present (Re=4000). Dash-dot lines with symbols: NASA QFF experiment[36,38] (Re=1.66×10^5) .

Although the flow Reynolds number of the present computation is much lower than the experiment, we try to compare the acoustic result with the available experimental measurement[36,38]. Since the present prediction is performed for the small span width (L_z=3D), it should be corrected for actual long span (L=16D) for the comparison, and this requires the span-wise coherent length scale information. We adapt the span-wise coherent length data provided with the experiment[36], and it is found that the span-wise coherent length is longer than the simulated span width only at the dominant shedding frequency. Based on the correction formulation proposed by Seo and Moon[7], it results in a +9.4 [dB] correction at the dominant shedding frequency and a +7.2 [dB] correction for other frequencies. The corrected PSDs are plotted with the experimental data in Fig. 7. Because of different Reynolds number in the present simulation and the experiment, the spectra do not match with each other well, especially for the peak frequency and overall amplitude. However, some qualitative agreement is notable. For example, at point **A**, there are

notable peaks at the both second and third harmonics, but at point **B**, the peak at the third harmonics is only well exhibited, and at point **C**, the peak at the second harmonics is only well represented. A better agreement with the measured frequency and amplitude is expected for simulation at higher Reynolds number.

B. Preliminary Result of Rudimentary Landing Gear Noise

In this section, the noise generated by flow over a rudimentary landing gear[42] configuration is considered in order to demonstrate the capability of the current solver to address problems with highly complex geometries. Only preliminary results at early stage of computation are presented here. The geometry of landing gear is based on the Ref[42]. The landing gear shape is generated by surface meshes with total 187742 triangular elements and shown in Fig. 8a. The landing gear is placed in the rectangular domain: $0 \leq x \leq 12D$, $0 \leq y \leq 6D$, $0 \leq z \leq 5D$, (where D is the diameter of wheel) and non-uniform Cartesian grid with total $512 \times 256 \times 256$ (about 33 million) grid points is used. The computational grid in x-y plane is shown in Fig. 8b. For the present test computation, the Reynolds number based on the wheel diameter and flow Mach number are set to Re_D=2000 and M=0.3, respectively. Figure 9a shows instantaneous vortical structures with Q-criteria (Eq. 13) and complex three-dimensional vortex structures are observed in the landing gear wake. The instantaneous acoustic field is plotted in Fig. 9b with total pressure fluctuation (Eq. 12) contours at several planes. It shows radiating acoustic waves as well as the pressure fluctuations caused by vortices in the wake.

a   b
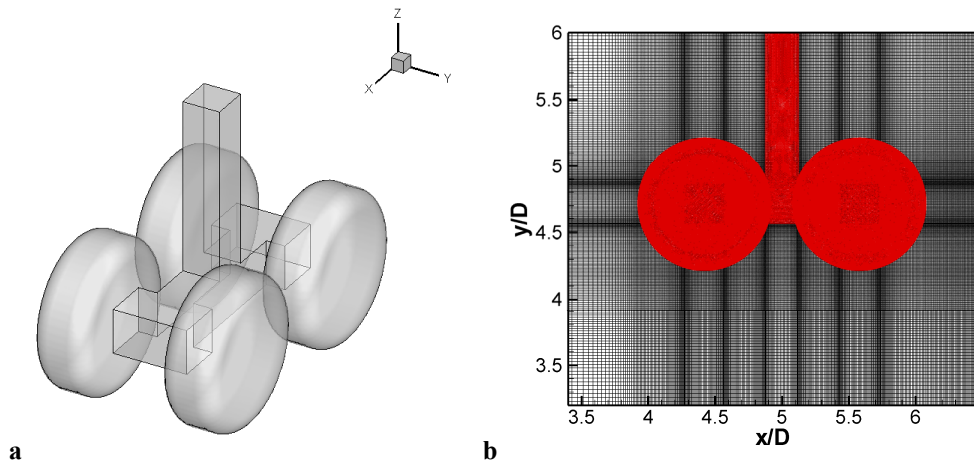
Figure 8. a) Geometry of rudimentary landing gear. b) Computational grid in *x-y* plane around the landing gear.

a   b
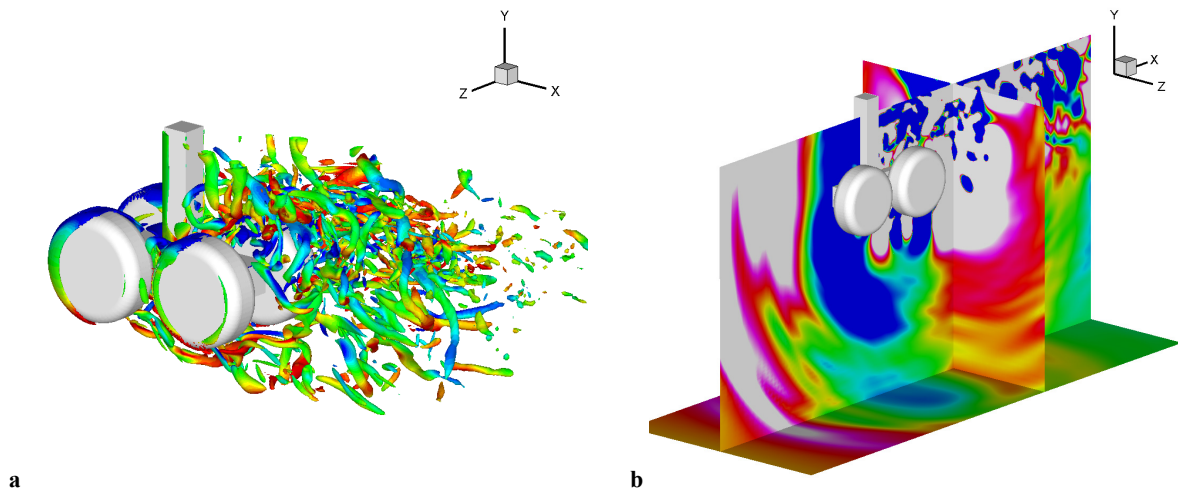
Figure 9. Instantaneous flow and acoustic field; a) Vortical structures colored by span-wise vorticity. b) Total pressure fluctuation contours.

C. Sound Generated by Flapping Motion

In order to test the present method for a moving body problem with relatively complex geometrical configuration, the sound generated flapping wings is considered in this section. The problem is relevant to the aerodynamic sound generation in the flight of an insect or a MAV with flapping wings. The schematic of the problem is shown in Fig. 10a. The main body and wings are modeled by canonical geometries and the flapping motion of wings is prescribed with the sinusoidal time variation of the angular velocity:

$$\dot{\theta} = V_{max} / r_{tip} \sin(2\pi t / T) , \qquad (14)$$

where V_{max} is the maximum wing tip velocity, $r_{tip}=1.5c$ is the distance from the body center to the wing tip, and T is the period. The wing length c and the maximum wing tip velocity V_{max} are used as the length and velocity scales, respectively. Left and right wings move symmetrically with a simple sinusoidal motion. The Reynolds number is set to 200, the Strouhal number is $c/TV_{max}=0.25$, and the Mach number based on the wing tip velocity is M=0.1. A Cartesian grid with 512×512 points is used and the wing length c is resolved by about 60 grid points. The instantaneous flow field is shown by the vorticity contour in Fig. 10b. Time histories of lift coefficients for wing and body are plotted in Fig. 11. Due to the symmetry, the lift coefficients of left and right wings are the same. The lift coefficient of the body also varies in time due to the induced flow by flapping motions.
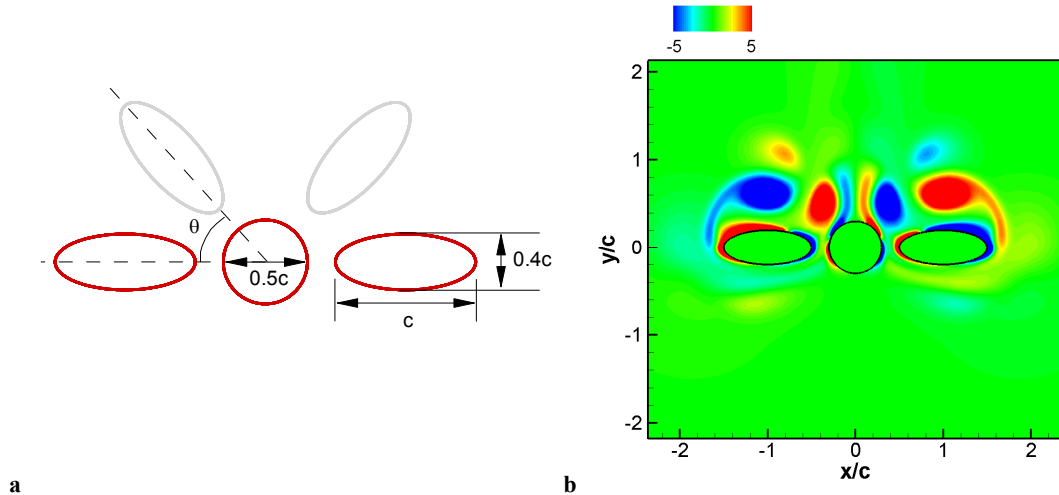
Figure 10. a) schematic of modeled flapping motion. b) Instantaneous vorticity contours
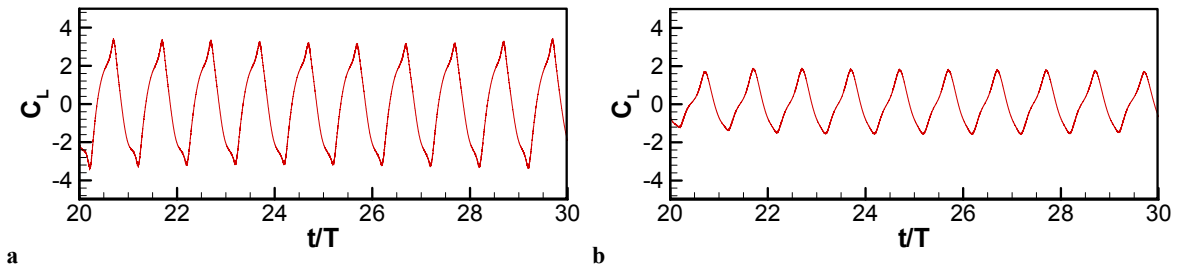
Figure 11. Time histories of lift coefficients; a) wings, b) center body.

The acoustic field is computed by LPCE and Fig. 12a shows the instantaneous field. Based on the Strouhal and Mach number, the wavelength of the main wave is 40c. The symmetric flapping motion of two wings behaves like a dipole sound source, and the directivity pattern shown in Fig. 12b shows a dipole in the vertical direction. Time histories of acoustic pressure monitored at (0,60c) and (0,-60c) are plotted in Fig. 13. The signal is periodic and particular wave forms are interesting. Although the present problem employs simple geometry and motion, it illustrates the capability of the present method for resolving sound generation by moving bodies quite well. The realistic three-dimensional geometry and flapping motion in insect flight will be considered in the future study.
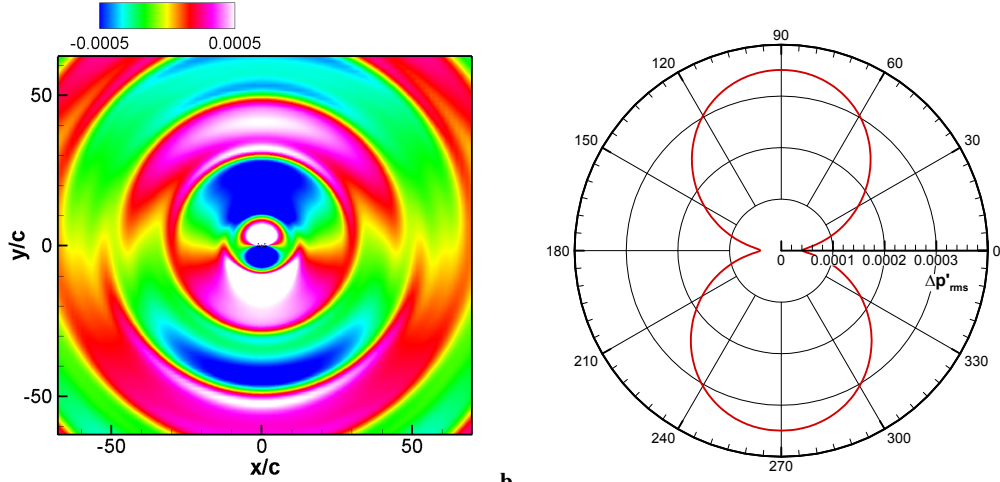
Figure 12. a) Instantaneous acoustic field generated by a modeled flapping motion. b) directivity at *r*=50*c*.
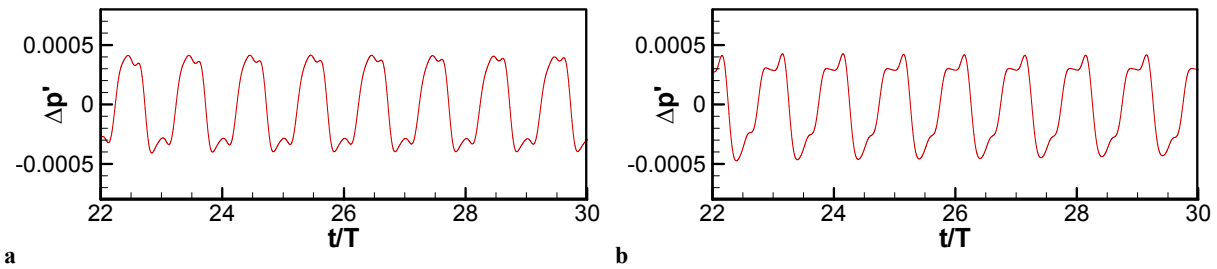
Figure 13. Time histories of acoustic pressure fluctuation monitored at a) (0,60*c*) and b) (0,-60*c*).

IV.   Conclusion

In this paper, the computation of aerodynamic sound at low Mach numbers around complex, stationary and moving bodies have been described for several modeled and practical problems. The flow-field and sound generation and propagation around very complex geometries with arbitrary body motion are predicted with an IBM based INS/LPCE hybrid method on the non-body conformal Cartesian grids. The present approach is quite versatile and applicable to the prediction of airframe noise at low sub-sonic speed, fan noise in industrial turbo machineries as well as electric devices, and many other aerodynamic noise problems in practical applications. One challenge is that resolution of flows at very high Reynolds number on a Cartesian grid is very costly. This issue is being addressed by employing local grid refinement strategy.

Acknowledgement

References

[1]Colonius, T. and Lele, S. K. "Computational aeroacoustics: progress on nonlinear problems of sound generation," *Progress in Aerospace Sciences*, Vol. 40, No. 6, 2004, pp. 345-416.

[2]Bailly, C., Bogey, C., and Marsden, O., "Progress in direct noise computation," *International Journal of Aeroacoustics*, Vol. 9, 2010, pp. 123-143.

[3]Lilley, G. M., "The prediction of airframe noise and comparison with experiment," *Journal of Sound and Vibration*, Vol. 239, No. 4, 2001, pp. 849-859.

[4]Wang, M. and Moin, P., "Computation of trailing-edge noise using large-eddy simulation," *AIAA Journal*, Vol. 38, No. 12, 2000, pp. 2201-2209.

[5]Ewert, R. and Schroder W., "On the simulation of trailing edge noise with hybrid LES/APE method," *Journal of Sound and Vibration*, Vol. 270, No. 3, 2004, pp. 509-524.

[6]Terracol, M., Manoha, E., Herrero, C., Labourasse, E., Redonnet, S., and Sagaut, P., "Hybrid methods for airframe noise numerical prediction," *Theoretical and Computational Fluid Dynamics*, Vol. 19, No. 3, 2005, pp. 197-227.

[7]Seo, J. H. and Moon, Y. J., "Aerodynamic Noise Prediction for Long-span Bodies," *Journal of Sound and Vibration*," Vol. 306, 2007, pp. 564-579.

[8]Greshner, B., Thiele, F., Jacob, M. C., and Casalino, D., "Prediction of sound generated by a rod-airfoil configurations using EASM DES and generalized Lighthill/FW-H analogy," *Computers and Fluids*, Vol. 37, No. 4, 2008, pp. 402-413.

[9]Moon, Y. J., Seo, J. H., Bae, Y. M., Roger, M., and Becker, S., "A hybrid prediction for low-subsonic turbulent flow noise," *Computers and Fluids*, Vol. 39, 2010, pp. 1125-1135.

[10]Lockard, D. P., Khorrami, M. R., Li, F., "Aeroacoustic analysis of a simplified landing gear," AIAA Paper 2003-3111, 2003.

[11]Souliez, F. J., Long, L. N., Morris, P. J., and Sharma, A., "Landing gear aerodynamic noise prediction using unstructured grid," *International Journal of Aeroacoustics*, Vol. 1, No. 2, 2002, pp. 115-135.

[12]Terracol, M., Labourasse, E., Manoha, E., "Simulation of the 3D unsteady flow in a slat cove for noise prediction," AIAA Paper 2003-3110, 2003.

[13]Ewert, R., "Broadband slat noise prediction based on CAA and stochastic sound sources from a fast random particle-mesh (RPM) method," *Computers and Fluids*, Vol. 37, No. 4, 2008, pp. 369-387.

[14]Manoha, E., Guenanff, R., Redonnet, S., and Terracol, M., "Acoustic scattering from complex geometries," AIAA Paper 2004-2938, 2004.

[15]Sherer, S. E. and Scott, J. N., "High-order Compact Finite Difference methods on General Overset Grids," *Journal of Computational Physics*, Vol. 210, 2005, pp. 459-496.

[16]Sherer, S. E. and Visbal, M. R., "High-order Overset-grid Simulations of Acoustic Scattering from Multiple Cylinders," Proc. of the Fourth Computational Aeroacoustics (CAA) Workshop on Benchmark Problems, NASA/CP-2004-212954, pp. 255-266.

[17]Hu, F. Q., Hussaini, M. Y., and Rasetarinera, P., "An Analysis of the Discontinuous Galerkin for Wave Propagation Problems," *Journal of Computational Physics*, Vol. 151, 1999, pp. 921-946.

[18]Chevaugeon, N., Hillewaert, K., Gallez, X., Ploumhans, P., and Remacle, J.-F., "Optimal Numerical Parameterization of Discontinuous Galerkin Method applied to Wave Propagation Problems," *Journal of Computational Physics*, Vol. 223, 2007, pp. 188-207.

[19]Dumbser, M, and Munz, C.-D., "ADER Discontinuous Galerkin Schemes for Aeroacoustics," *C.R.Mecanique*, Vol. 333, 2005, pp. 683-687.

[20]Toulorge, T, Reymen, Y., and Desmet, W., "A 2D Discontinuous Galerkin Method for Aeroacoustics with Curved Boundary Treatment," Proc. of International Conference on Noise and Vibration Engineering (ISMA2008), pp. 565-578.

[21]Cand, M., "3-Dimensional Noise Propagation using a Cartesian Grid," AIAA Paper, 2004-2816, 2004.

[22]Liu, Q. and Vasilyev, O. V., "A Brinkman Penalization Method for Compressible Flows in Complex Geometries," *Journal of Computational Physics*, Vol. 227, 2007, pp. 946-966.

[23]Arina, R. and Mohammadi, M., "An Immersed Boundary Method for Aeroacoustics Problems," AIAA Paper, 2008-3003, 2008.

[24]Liu, M. and Wu, K., "Aerodynamic Noise Propagation Simulation using Immersed Boundary Method and Finite Volume Optimized Prefactored Compact Scheme," *J. Therm. Sci.* Vol. 17, No. 4, 2008, pp. 361-367.

[25]Seo, J. H., and Mittal, R., "A High-Order Immersed Boundary Method for Acoustic Wave Scattering and Low-Mach number Flow-induced Sound in Complex Geometries," *Journal of Computational Physics*, 2010, doi:10.1016/j.jcp.2010.10.017.

[26]Mittal, R. and Iaccarino, G., "Immersed Boundary Methods," *Annu. Rev. Fluid Mechanics*, Vol. 37, 2005, pp. 239-261.

[27]Hardin, J. C., and Pope, D. S., "An Acoustic/Viscous Splitting Technique for Computational Aeroacoustics," *Theoret. Comput. Fluid Dynamics*, Vol. 6, 1994, pp. 323-340.

[28]Seo, J. H., and Moon, Y. J., "The Perturbed Compressible Equations for Aeroacoustic Noise Prediction at Low Mach Numbers," *AIAA Journal*, Vol. 43, No. 8, pp. 1716-1724, 2005.

[29]Seo, J. H. and Moon, Y. J., "Linearized Perturbed Compressible Equations for Low Mach Number Aeroacoustics," *Journal of Computational Physics*, Vol. 218, 2006, pp. 702-719.

[30]Mittal, R., Dong, H., Bozkurttas, M., Najjar, F. M., Vargas, A., and von Loebbecke, A., "A Versatile Sharp Interface Immersed Boundary Method for Incompressible Flows with Complex Boundaries," *Journal of Computational Physics*, Vol. 227, 2008, 4825-2852.

[31]Ghias, R., Mittal, R., Dong, H., ""A Sharp Interface Immersed Boundary Method for Compressible Viscous Flows," *Journal of Computational Physics*, Vol. 225, 2007, pp. 528-553.

[32]Luo, H., Mittal, R., Zheng, X., Bielamowicz, S. A., Walsh, R. J., and Hahn, J. K., "An Immersed-Boundary Method for Flow-Structure Interaction in Biological Systems with Application to Phonation," *Journal of Computational Physics*, Vol. 227, 2008. pp. 9303-9332.

[33]Lele, S. K., "Compact Finite Difference Schemes with Spectral-like Resolution," *Journal of Computational Physics*, Vol. 103, 1992, pp. 16-42.

[34]Gaitonde, D., Shang, J. S., and Young, J. L., "Practical Aspects of Higher-order Accurate Finite Volume Schemes for Wave Propagation Phenomena," *International Journal for Numerical Methods in Engineering*, Vol. 45, 1999, pp. 1849-1869.

[35]Udaykumar, H. S., Mittal, R., Rampunggoon, P., and Khanna, A., "A Sharp Interface Cartesian Grid Method for Simulating Flows with Complex Moving Boundaries," *Journal of Computational Physics*, Vol. 174, 2001, pp. 345-380.

[36]Lockard, D. P. "Tandem Cylinder Benchmark Problem," Workshop on Benchmark Problems on Airframe Noise (BANC)-I, Problem 2: http://groups.google.com/group/afnworkshop_problem2.

[37]Lockard, D., Khorrami, M., and Choudhari, M., "Tandem Cylinder Noise Predictions," 13th AIAA/CEAS Aeroacoustic Conference, 2007, AIAA Paper 2007-3450.

[38]Khorrami, M. R., Choudhari, M. M., Lockard, D. P., Jenkins, L. N., and McGinley, C. B., "Unsteady Flowfield around Tandem Cylinders as Prototype Component Interaction in Airframe Noise," *AIAA Journal*, Vol. 45, No. 8, 2007, pp. 1930-1941.

[39]Papaioannou, G. V., Yue, D. K. P., Triantafyllou, M. S., and Karniadakis, G. E., "Three-dimensionality Effects in Flow around Two Tandem Cylinders," *Journal of Fluid Mechanics*, Vol. 558, 2006, pp. 387-413.

[40]Igarashi, T., "Characteristics of the Flow around Two Circular Cylinders arranged in Tandem, 1st Report," *Bull. JSME*, Vol. B27, No. 233, 1981, pp. 2380-2387.

[41]Oberai, A. A., Roknaldin, F., and Hughes, T. J. R., "Trailing-edge Noise due to Turbulent Flows," Technical Report, No. 02-002, Boston University, 2002.

[42]Spalart, P., Shur, M., Strelets, M., and Travin, A., "Initial RANS and DDES of a Rudimentary Landing Gear," *Notes on Numerical Fluid Mechanics and Multidisciplinary Design*, Vol. 111, 2010, pp. 101-110.